Energy Conversion and Management 344 (2025) 120266

Contents lists available at ScienceDirect

Energy Conversion and Management

journal homepage: www.elsevier.com/locate/enconman

Research Paper

Temperature-voltage characteristics and theoretical limit of exergy efficiency for CPV/T systems

Yuan Gao, Entao Zhang, Yin Xie, Xuan Zhu, Chenyu Xu, Yanwei Zhang *

State Key Laboratory of Clean Energy Utilization, Zhejiang University, Hangzhou 310027, China

A B S T R A C T

As the core of theoretical modeling for concentrated photovoltaic and thermal (CPV/T) systems, carrier balance (CB) and lattice thermal equilibrium (TE) in semiconductors are typically coupled solely at the maximum power point (MPP) of CPVs. Here, we demonstrate that this single-point coupling approach, derived from the Shockley model, introduces significant inaccuracies as it fails to capture the temperature-voltage (TV) characteristics of CPV/T systems. To address this limitation, a full-voltage-range coupling model (FRCM) is developed. This model reveals pronounced TV characteristics in CPV/T systems, resulting from voltage-dependent variations of CB-TE coupling induced by concentrated radiation, which are validated by experimental data. The TV characteristic markedly influences the current–voltage characteristic and total exergy efficiency (η_{total}) of CPV/T systems through CB-TE coupling and results in a maximum exergy point distinct from the MPP. Using the FRCM, universal principles for enhancing η_{total} through heat transfer adjustments are identified. Based on these principles, the theoretical limit for η_{total} of an ideal CPV/T system is established. Wide-range calculations indicate that the theoretical η_{total} can exceed 56 %. This work deepens the fundamental understanding of CPV/T systems and provides a robust framework for guiding optimization, contributing to unlocking their potential as highly efficient and sustainable energy solutions.

1. Introduction

Concentrated photovoltaic and thermal (CPV/T) systems remove heat of CPVs by enhancing heat transfer and thus simultaneously improve the output of electricity and thermal exergy, which effectively enhances the total exergy efficiencies (η_{total}) of converting solar energy [1–3]. As the η_{total} of advanced CPV/T systems has reached 33.9 % [4], slightly surpassing the Shockley–Queisser limit for single-junction photovoltaics, developing robust theoretical models and exploring the theoretical limits of η_{total} are critical for driving further advancements. The core of CPV/T systems modeling lies in understanding the behavior of semiconductors under concentrated radiation. The role of the lattice in concentrated semiconductors becomes critical because elevated temperature of semiconductors (T_{sem}) intensifies its vibrations [5]. Consequently, carrier balance (CB), lattice thermal equilibrium (TE), and the coupling between CB and TE are three essential physical processes in concentrated semiconductors at a steady state. Substantial theoretical progress has been made in these three processes. The Shockley model established CB for calculating the current–voltage (IV) characteristics of photovoltaics under non-concentrated radiation [6]. In concentrated semiconductors, however, CB must account for the effects of T_{sem} on bandgap and carrier dynamics, which has been addressed by refinements to the Shockley model [7–9]. TE is defined as the equilibrium between thermal source terms and thermal output terms in semiconductors. The thermal output terms can be accurately modeled through heat transfer analysis [10,11]. The coupling between CB and TE has been summarized into two relationships: T_{sem} in CB is determined by TE [12,13], and the thermal source terms in TE originate from physical processes in CB, which generate thermal energy through electroacoustic interactions [14,15].

Despite foundational progress, current models of CPV/T systems exhibit theoretical shortcomings, particularly in the CB-TE coupling. Specifically, existing models are the single-point coupling model (SPCM), where CB and TE are coupled only at the maximum power point (MPP) of the CPV [16–18]. This coupling approach contradicts the physical reality that interactions between carriers and the lattice persist continuously in concentrated semiconductors. Moreover, the single-point coupling is fundamentally based on the assumption that T_{sem} at all other voltages is equal to T_{sem} at V_{MPP} [19]. This is because, although TE and CB are coupled only at MPP, the determination of MPP still requires the complete IV characteristic [20]. When using CB to calculate the IV characteristic at other voltages, T_{sem} in CB can only be assumed to be equal to T_{sem} at V_{MPP}, as it is the only value of T_{sem} obtainable through coupling TE. However, the validity of this assumption in SPCM has received minimal scrutiny. This is likely due to its alignment with the implicit assumption in the Shockley model, which assumes that T_{sem} remains constant with voltage under non-concentrated radiation [6]. In

* Corresponding author.
E-mail address: zhangyw@zju.edu.cn (Y. Zhang).

https://doi.org/10.1016/j.enconman.2025.120266
Received 19 May 2025; Received in revised form 4 July 2025; Accepted 20 July 2025
Available online 8 August 2025

Nomenclature

E_{ele}	power of extracted carriers
E_{g0}	bandgap of semiconductor catalysts
E_g	bandgap of semiconductor catalysts at 298.15 K
E_{in}	the incident solar power
E_{iso}	power of isothermal dissipation
E_{nonrad}	power of non-radiative recombination
E_{rad}	power of radiative recombination
E_S	power of excited carriers
E_{the}	power of thermalization
F_{nonrad}	non-radiative recombination rate of carriers
F_{rad}	radiative recombination rate of carriers
F_s	excitation rate of carriers
I	current of photovoltaics
q	elementary charge
Q_{con}	convective heat transfer power
$Q_{conduction}$	conductive heat transfer power
Q_{rad}	radiative heat transfer power
Q_{rec}	reaction heat power
Q_{source}	thermal source power
T_0	ambient temperature, 298.15 K
T_{gap}	difference between T_{sem} and T_{outlet}
T_{outlet}	the outlet temperature of HTF
T_{sem}	temperature of semiconductor catalysts
V	voltage of photovoltaics
$\Delta E_{ele-MEP}$	rise in electricity at MEP
$\Delta Q_{con-MEP}$	reduction in thermal energy at MEP
$\Delta Q_{x-con-MEP}$	reduction in thermal exergy at MEP
η_{Carnot}	efficiency of the Carnot cycle
η_{Eele}	ratio of E_{ele} to the incident solar power
η_{ele}	electricity efficiency
$\eta_{Qsource}$	ratio of Q_{source} to the incident solar power
$\eta_{Shockley}$	Shockley-Queisser limit of efficiency
$\eta_{thermal}$	thermal exergy efficiency
η_{total}	total exergy efficiency

Abbreviations

C	concentration ratio
CB	carrier balance
CPV/T	concentrated photovoltaic/thermal
FF	fill factor
FRCM	full-voltage-range coupling model
H	height of the microchannel
HTF	heat transfer fluid
IV	current–voltage
MEP	maximum exergy point
MPP	maximum power point
OC	Open-circuit
PTC	photothermal chemistry
SPCM	single-point coupling model
TE	lattice thermal equilibrium
TV	temperature-voltage

concentrated semiconductors, nevertheless, it remains unclear whether the assumption is still valid. Addressing these questions requires a full-voltage-range coupling model (FRCM) that couples CB and TE across the entire operating voltage range.

In addition to theoretical shortcomings, the exploration of the theoretical limit for η_{total} of CPV/T systems remains inadequate. The theoretical limit of η_{total} defines the maximum capability of CPV/T systems to convert input solar energy into exergy, which is established by optimizing heat transfer conditions when semiconductor properties and input energy are set. Nonetheless, some models are tailored to specific CPV/T devices, and the variation of T_{sem} is constrained by the thermal tolerance of photovoltaic materials or other system components, which restricts the scope of heat transfer adjustment and undervalues the contribution of $\eta_{thermal}$ to η_{total} [21–23]. Therefore, these models typically predict theoretical η_{total} values below 40 %, which represent only marginal potential enhancements beyond the Shockley–Queisser limit. In fact, advancements in material science have significantly enhanced the thermal tolerance of CPV devices. Some III–V photovoltaics can withstand temperatures exceeding 723 K [24–26], and even some next-generation photovoltaics also exhibit thermal tolerance above 473 K [27–29]. Models that incorporate a broader range of T_{sem} variations have broadened the scope of heat transfer adjustment and demonstrated theoretical η_{total} values exceeding 40 %. However, the incomplete application of existing theoretical frameworks often leads to insufficient self-consistency and physical interpretability. For instance, in some cases, T_{sem} is artificially assigned rather than being derived from TE [30,31], or empirical parameters, such as the temperature coefficient of η_{ele}, are employed to replace the construction of CB [17,32]. These simplifications make the effects of heat transfer adjustment on CB, TE, and CB-TE coupling unidentifiable, thereby impeding the exploration of universal principles governing heat transfer adjustment and the theoretical limits of η_{total}.

In this study, an FRCM that couples CB and TE across the entire operating voltage range is developed. This model reveals pronounced TV characteristics in CPV/T systems, resulting from voltage-dependent variations of CB-TE coupling induced by concentrated radiation, which are validated by experimental data. The TV characteristic substantially influences the IV characteristic and η_{total} of CPV/T systems through CB-TE coupling and results in a maximum exergy point that differs from the MPP. In contrast, the SPCM introduces significant inaccuracies, as its constant T_{sem} assumption fails to capture TV characteristics and their effects on IV characteristics. Using the FRCM, universal principles for enhancing η_{total} of CPV/T systems through heat transfer adjustments are explored, and the theoretical limit for η_{total} of an ideal CPV/T system is established based on these principles. Calculations across a wide range of bandgaps and concentration ratios demonstrate that the theoretical η_{total} of CPV/T systems can exceed 56 %. This work emphasizes the vast potential of CPV/T systems for efficiently converting solar energy into exergy, laying a robust foundation for advancing the understanding and optimization of CPV/T systems.

2. Full-range coupling model

2.1. CB

The ideal CPV/T device in this study is shown in Fig. 1a. The FRCM is established by coupling CB and TE across the entire operating voltage range, and the existing theoretical framework is applied comprehensively. The CB with temperature effects is expressed as: [6]

$$F_s(T) - F_{rad}(V,T) - F_{nonrad}(V,T) - \frac{I(V,T)}{q} = 0 \tag{1}$$

Here, F_s, F_{rad}, F_{nonrad}, are the rates of carrier generation, radiative recombination, and nonradiative recombination, respectively.I, V, and q denote the current to the external circuit, the voltage of CPV, and the elementary charge, respectively. All terms are functions of T_{sem} and the bandgap [20], with the bandgap also being a function of T_{sem} [33,34] (Supplementary Note 1, Supplementary Fig. 1). F_{nonrad} is zero for the ideal CPV. The calculation methods for F_s, F_{rad} are detailed in

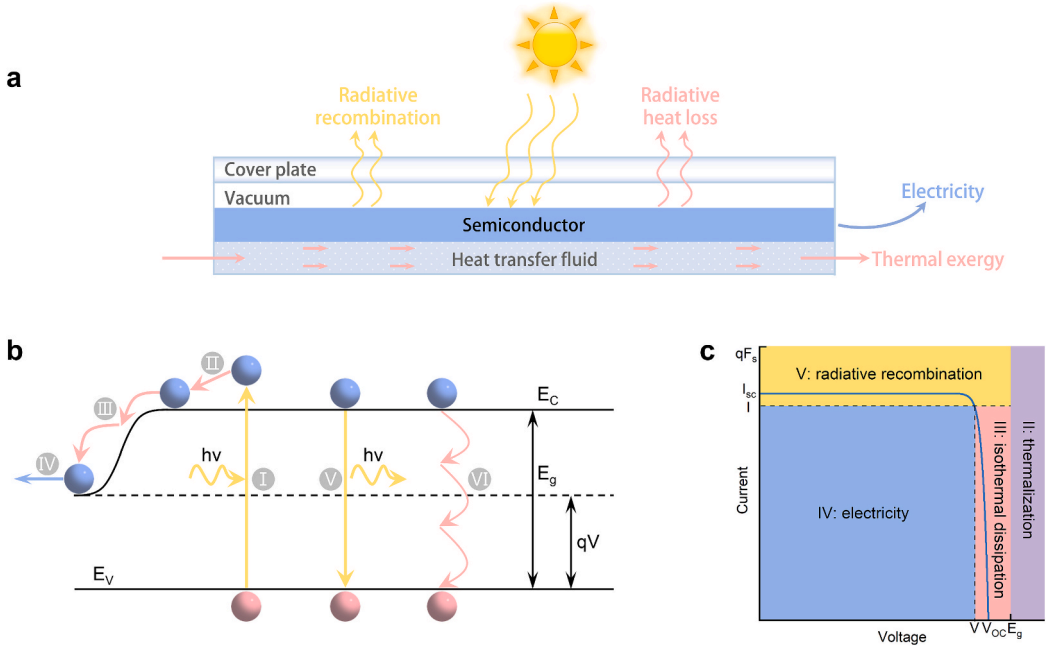

Fig. 1. Schematic of the ideal CPV/T device and CB in semiconductors. (a) The schematic of the ideal CPV/T device in this work. There is a vacuum between the CPV and the transparent cover plate, and the heat transfer fluid flows through microchannels beneath the CPV to carry away the heat. A more detailed introduction is provided in Supplementary Note 4. (b) Carrier dynamics within the semiconductor, including I) carrier excitation, II) thermalization, III) isothermal dissipation: A portion of the energy of the extracted carriers to the external circuit is dissipated as heat due to the difference between E_g and V. IV) extraction and utilization, V) radiative recombination: an electron in the conduction band recombines with a hole in the valence band, and the excess energy is emitted in the form of a photon. VI) non-radiative recombination: electrons and holes recombine and release phonons instead of photons. The yellow and pink arrows represent the absorption (emission) of photons and phonons, respectively. The phonons are not explicitly depicted. (c) Energy diagram of Processes II-V in (b), and the blue line is the IV curve. Process VI is not depicted, as non-radiative recombination is zero in an ideal semiconductor. The sum of energy from Processes II to V is the total energy of excited carriers in Process I. F_s, I_{SC}, E_g and V_{OC} are the rates of carrier generation, short-circuit current, bandgap, and open-circuit voltage, respectively.

Supplementary Note 2. Since $F_{rad}(V,T)$ has a critical influence on CB, it is described explicitly as follows:

$$F_{rad}(V,T) = F_{rad}(0,T_0)\left(\frac{T}{T_0}\right)^3 exp[\frac{E_{g0}}{kT_0} - \frac{E_g(T)}{kT}]exp\left(\frac{qV}{kT}\right) \quad (2)$$

Here, T_0 is ambient temperature, set at 298.15 K unless otherwise specified. $F_{rad}(0,T_0)$ represents the radiative recombination rate at T_0 under no illumination. E_{g0} and $E_g(T)$ are bandgap when T_{sem} at T_0 and T, respectively, and k is the Boltzmann constant.

2.2. TE and CB-TE coupling

The energy conservation in the semiconductor can be established based on CB:

$$E_S(T) = E_{the}(V,T) + E_{iso}(V,T) + E_{ele}(V,T) + E_{rad}(V,T) + E_{nonrad}(V,T) \quad (3)$$

E_S, E_{the}, E_{iso}, E_{ele}, E_{rad}, E_{nonrad} are powers of excited carriers, thermalization, isothermal dissipation, electricity, radiative recombination, and non-radiative recombination, respectively [35]. The diagrams of each term in Eq. (3) are shown in Fig. 1b-c, with detailed formulas provided in Supplementary Note 3. The isothermal dissipation is rarely mentioned in the literature, so a more detailed explanation is provided here. Carriers extracted to the external circuit experience the isothermal dissipation process, and the contribution of a single carrier is the difference between E_g and qV (III process in Fig. 1b). Therefore, E_{iso} is calculated as [36]:

$$E_{iso}(V,T) = I(V,T)\left[E_g(T) - V\right] \quad (4)$$

The first CB-TE coupling relationship is that T_{sem} in CB is calculated by TE. The TE in the semiconductor is given by [37],

$$Q_{source}(T) = Q_{conduction}(T) + Q_{con}(T) + Q_{rad}(T) \quad (5)$$

Thermal output terms include $Q_{conduction}$, Q_{con} and Q_{rad}, which correspond to the power of conduction, convection, and radiation heat transfer, respectively. CPV/T systems typically utilize the thermal energy in conduction and convection heat transfer. Although the Q_{rad} in high temperature can be harnessed in devices like thermophotovoltaics, it is generally considered to be unexploitable in CPV/T systems [38]. In this study, an ideal CPV/T system is designed to utilize only convective heat transfer to extract thermal energy (Fig. 1a). High-temperature thermal oil [39], serving as the heat transfer fluid (HTF), flows through microchannels to remove heat of CPV. Q_{con} and Q_{rad} of the system are established as functions of T_{sem} through heat transfer analysis (Supplementary Note 4).

The second CB-TE coupling relationship is that thermal source terms in TE originate from CB. Three processes in CB generate thermal energy via electroacoustic interactions, including thermalization, isothermal dissipation, and non-radiative recombination. Current models commonly adopt an indirect definition of Q_{source}, [40,41]

$$Q_{source} = E_S(T) - E_{ele}(V,T) - E_{rad}(V,T) \quad (6)$$

The indirect definition renders the individual variations of three thermal source terms implicit, which is unfavorable for the analysis of interactions between CB and TE. To overcome this limitation, we adopt a direct definition of Q_{source} in this work:

$$Q_{source} = E_{the}(V,T) + E_{nonrad}(V,T) + E_{iso}(V,T) \quad (7)$$

External heat sources can also be included in Q_{source} if present. Therefore, the TE in the semiconductor is

$$E_{the}(V,T) + E_{nonrad}(V,T) + E_{iso}(V,T) = Q_{conduction}(T) + Q_{con}(T) + Q_{rad}(T) \quad (8)$$

This expression reveals that the thermal source terms originating from

CB vary with voltage, resulting in changes of TE and T_{sem} with voltage. This theoretically indicates the existence of TV characteristics in CPV/T systems, analogous to IV characteristics. The FRCM is established by simultaneously solving Eqs. (3) and (8) across the entire operating voltage range. A computational framework is constructed to implement this process (Supplementary Fig. 2), which is executed using MATLAB. For comparison, an SPCM is also developed, with its computational framework detailed in Supplementary Fig. 3.

The electricity efficiency (η_{ele}), thermal exergy efficiency ($\eta_{thermal}$), and η_{total} are defined as

$$\eta_{ele} = \frac{E_{ele}}{E_{in}} \tag{9}$$

$$\eta_{thermal} = \frac{Q_{con} \times \left[1 - \left(\frac{T_0}{T_{outlet}}\right)\right]}{E_{in}} \tag{10}$$

$$\eta_{total} = \eta_{ele} + \eta_{thermal} \tag{11}$$

E_{in} is the power of input solar energy, and T_{outlet} is the outlet temperature of HTF. The proportion of thermal energy converted into exergy is determined by the efficiency of the Carnot cycle.

3. TV characteristics in CPV/T systems

The FRCM was employed to analyze the performance of the CPV/T system under varying concentration ratios (C). E_{g0} was set to 1.34 eV, consistent with the optimal bandgap in the Shockley model [42]. The mass flow rate of the HTF and the height of the microchannel (H) were fixed at 1 kg/s and 500 μm, respectively. The FRCM revealed pronounced TV characteristics in the CPV/T systems, where T_{sem} decreases with increasing voltage (Fig. 2a). The TV characteristics arise because changes in CB with voltage lead to a reduction in the thermal source efficiency ($\eta_{Qsource} = \eta_{Eiso} + \eta_{Ethe}$) with rising voltages (Fig. 2b-c). Consequently, T_{sem} and the thermal output power (Q_{con} and Q_{rad}) decrease to maintain TE. The reduction in $\eta_{Qsource}$ is primarily attributed to a decrease in isothermal dissipation efficiency (η_{Eiso}). Specifically, the isothermal dissipation per carrier in CB diminishes at higher voltages (Equation (4)), and the number of carriers available for isothermal dissipation is also reduced at higher voltages because of the declining current caused by increased radiative recombination. The gradient of T_{sem} with respect to voltage ($\frac{dT_{sem}}{dV}$) intensifies as C rises (Fig. 2a). The difference in T_{sem} between V = 0 and open-circuit voltage (V_{oc}) reaches 643.8 K at C = 1000. The increasing $\frac{dT_{sem}}{dV}$ is attributed to the larger gradient of Q_{source} with respect to voltage ($\frac{dQ_{source}}{dV}$) at higher C (Supplementary Fig. 4). This trend arises because $\frac{d\eta_{Qsource}}{dV}$ increases with rising C (Fig. 2b-c, Supplementary Fig. 5), and the higher incident energy under greater C further amplifies this gradient ($Q_{source} = \eta_{Qsource} \times E_{in}$). This also explains that the constant T_{sem} assumption is valid under non-concentrated radiation because $\frac{dQ_{source}}{dV}$ can be neglected due to the low E_{in}.

The experimental data for actual CPVs were fitted using the FRCM to demonstrate the existence of TV characteristics. Literature data on AlGaInP CPV and GaInP CPV were selected considering their IV characteristics and recombination mechanisms are well-documented [43].

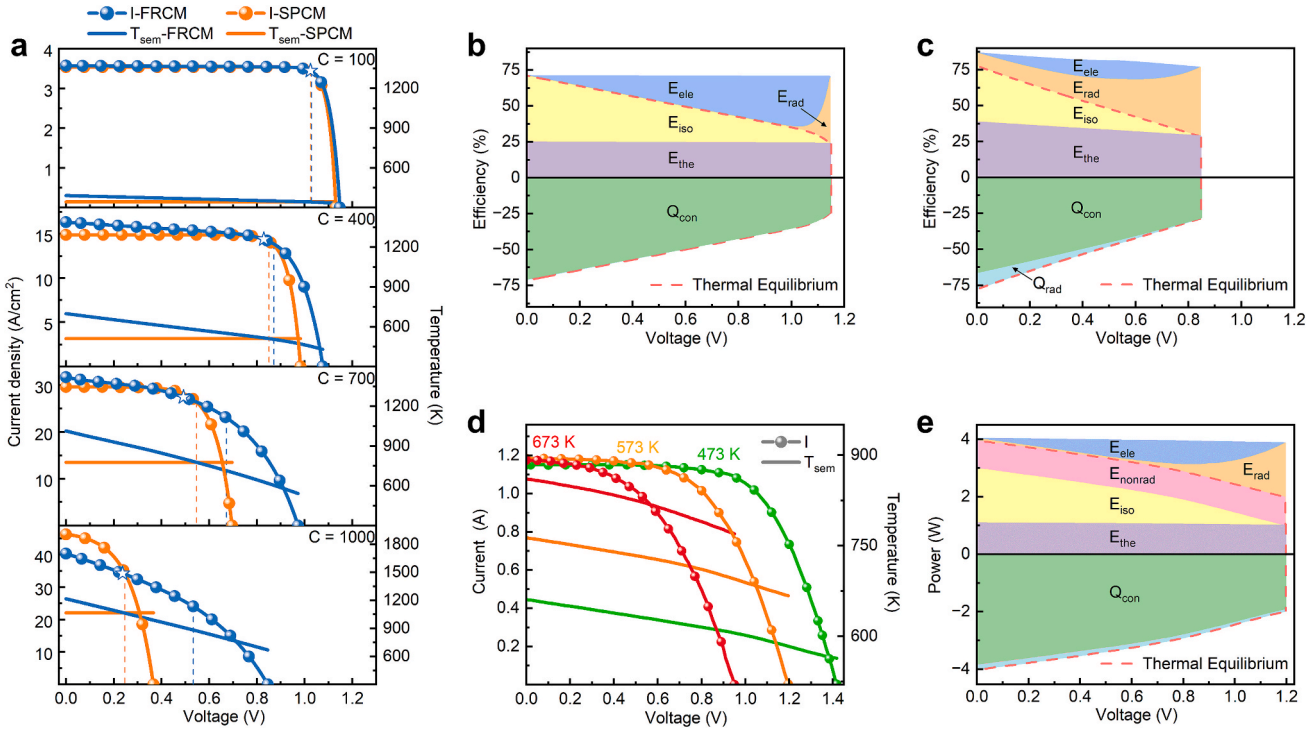

Fig. 2. TV characteristics of CPV/T systems. (a) IV and TV characteristics derived from the FRCM and SPCM under different C. Dashed droplines mark the MPPs on the IV curves, and pentagrams denote the maximum exergy points in FRCM. (b, c) Variations in the energy efficiencies of terms in CB and TE with voltage at (b) C = 100 and (c) C = 1000. The energy efficiency is defined as $\eta_x = \frac{E_x}{E_{in}}$, where x denotes a specific term. The region where y > 0 in (b) and (c) includes the energy efficiencies of all the output terms in the CB (E_{the}, E_{iso}, E_{ele}, and E_{rad}). The sum of them corresponds to the energy efficiency of E_S. Therefore, this region represents energy conservation of the CPV/T system (Eq. (3)). The area enclosed by the pink dashed lines indicates the TE of the CPV/T system. The region where y > 0 corresponds to the energy efficiencies of thermal source terms (E_{the}, and E_{iso}), while the region where y < 0 corresponds to the energy efficiencies of thermal output terms($Q_{conduction}$, Q_{con}, and Q_{rad}; see Eq. (8)), respectively. The label of Q_{rad} is omitted in (b) due to its negligible magnitude. Diagrams for C = 400 and C = 700 are presented in Supplementary Fig. 5. (d) IV characteristics and fitted TV characteristics of the AlGaInP CPV at C = 1000 with T_{stage} of 473 K, 573 K, and 673 K. (e) Variations in the energy efficiencies of terms in CB and TE with voltage for the AlGaInP CPV at T_{stage} = 573 K. Unlike the ideal CPV/T device, E_{nonrad} appears as a thermal source term here (see Eq. (8)).

The CPV was placed on a temperature-controlled stage, with the stage temperature (T_{stage}) varied from 473 K to 673 K, and C is fixed at 1000 [44]. Non-radiative recombination must be taken into account in actual CPVs. The dominant non-radiative recombination process in the AlGaInP and GaInP is thermionic emission, and the F_{nonrad} is assumed to be unaffected by TV characteristics, as variable temperature measurements have illustrated that it increases slowly with T_{sem} when T_{sem} exceeds T_0 [45]. Fitting details are provided in Supplementary Note 5. The fitting results confirm that AlGaInP and GaInP exhibit pronounced TV characteristics under all three T_{stage} (Fig. 2d, Supplementary Fig. 6). T_{sem} consistently exceeds T_{stage} due to the thermal effects of concentrated radiation. The observed $\frac{dT_{sem}}{dV}$ also primarily arises from the gradient of E_{iso} with respect to voltage (Fig. 2e, Supplementary Fig. 7). Compared to the ideal PV under the same radiation, the $\frac{dT_{sem}}{dV}$ of two kinds of CPVs is relatively small. This is because the relatively large E_{g0} (2.01 eV for AlGaInP and 1.90 eV for GaInP) and significant non-radiative recombination results in a smaller current, which reduces the gradient of E_{iso} with respect to voltage (Equation (4)). In addition, despite the constant non-radiative recombination with respect to voltage having minimal impact on $\frac{dT_{sem}}{dV}$, it significantly contributes to Q_{source} and increasing the overall T_{sem}. For instance, non-radiative recombination accounts for 24 % to 50 % of Q_{source} for AlGaInP CPV at T_{stage} = 573 K (Fig. 2e). These findings underscore the dual role of non-radiative recombination in CPV/T systems: it not only depletes carriers in CB but also acts as a significant heat source term in TE. This dual effect is crucial for optimizing real-world CPV/T devices, and the FRCM is a powerful tool to study it.

4. Comparisons between FRCM and SPCM

TV characteristics significantly influence the IV characteristics of CPV/T systems through the CB-TE coupling. Consequently, the SPCM leads to inaccuracies in IV characteristics due to the constant T_{sem} assumption. First, in the FRCM, the current begins to decrease from V = 0, which becomes particularly evident when C > 100. In comparison, the SPCM shows a relatively constant current before V_{MPP} (Fig. 2a). This discrepancy arises because the TV characteristic in the FRCM reflects the increase in E_g from V = 0, which leads to the reduction in absorbed photons with rising voltage (Supplementary Fig. 8). Additionally, the TV characteristics dictate that T_{sem} has a stronger enhancing effect on radiative recombination in the low-voltage region (Equation (2)), thereby negatively impacting the current in this region (Fig. 2c, Supplementary Fig. 5b). The constant T_{sem} in the SPCM fails to capture these two effects (Supplementary Figs. 8b, 9), so the current decreases only when radiative recombination becomes significant in the high-voltage region. Second, V_{oc} is underestimated in the SPCM (Fig. 3a). This occurs because T_{sem} is overestimated in the high-voltage region (Fig. 2a), which leads to an exaggerated radiative recombination rate (Supplementary Fig. 9), ultimately causing the current to reach zero more rapidly. The above two types of inaccuracies collectively make the IV curve of the SPCM closer to a rectangular shape, resulting in an overestimation of the fill factor (FF) compared to the FRCM (Fig. 3a). These deviations become more pronounced as C increases because the increasing $\frac{dT_{sem}}{dV}$ represents escalating errors of the constant T_{sem} assumption in the SPCM. At C = 1000, the errors in V_{oc} and FF can reach up to −0.48 V and 26.27 %, respectively. The exergy efficiencies also exhibit increasing deviations with rising C (Fig. 3b).

It is important to note that while CB and TE are coupled at V_{MPP} in the SPCM, this does not mean that the SPCM is accurate when considering only MPP performance. The CB-TE coupling indeed yields the correct values for the current and T_{sem} at V_{MPP}, as evidenced by both the IV and TV curves of the two models intersecting at the V_{MPP} of the SPCM (Fig. 2a). However, the V_{MPP} itself is inaccurate, and the error (the distance between two dashed lines in Fig. 2a) increases with C, reaching as much as −0.29 V when C = 1000. This error arises because the determination of the V_{MPP} relies on the accuracy of the overall TV and IV characteristics, rather than relying solely on the CB-TE coupling at V_{MPP}. This error can be quantitatively analyzed. Since T_{sem} is a function of

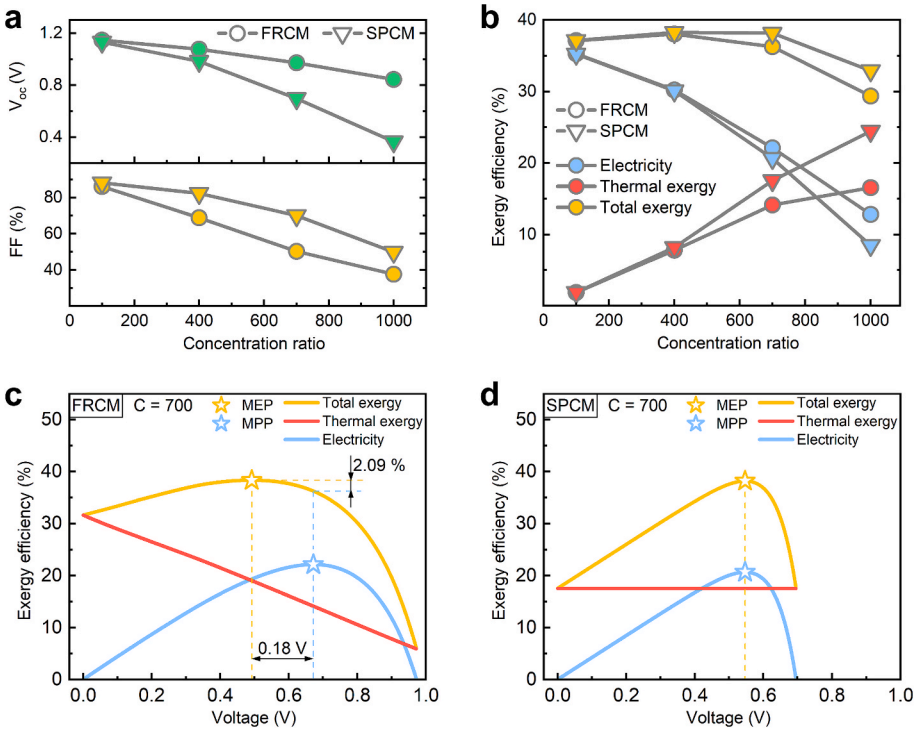

Fig. 3. The influence of TV characteristics on IV characteristics and the maximum exergy point of CPV/T systems. (a) Comparison of V_{oc} and FF in FRCM and SPCM. (b) Comparison of exergy efficiencies at MPP in two models. (c) Changes in exergy efficiencies with voltage in the FRCM at C = 700. (d) Changes in exergy efficiencies with voltage in the SPCM at C = 700.

voltage, the electrical power of the CPV/T system can be expressed as:

$$P = I[V, T(V)]V = P[V, T(V)] \tag{12}$$

The V_{MPP} is the voltage where the derivative of P is zero:

$$\frac{dP}{dV} = \frac{\partial P}{\partial V} + \frac{\partial P}{\partial T}\frac{dT}{dV} = 0 \tag{13}$$

T_{sem} can be considered constant with respect to voltage under non-concentrated conditions, allowing $\frac{\partial P}{\partial V} + \frac{\partial P}{\partial T}\frac{dT}{dV} = 0$ to simplify to $\frac{dP}{dV} = 0$, which is the equation used in the Shockley model to determine V_{MPP} [6]. However, the TV characteristics in CPV/T systems dictate that $\frac{dT}{dV}$ cannot be ignored. Therefore, the constant T_{sem} assumption in the SPCM leads to errors in V_{MPP}, which become more pronounced with rising C because of the increased $\frac{dT_{sem}}{dV}$.

5. Maximum exergy point of CPV/T systems

The FRCM can determine the maximum exergy point (MEP) of CPV/T systems and reveals that V_{MEP} is not identical to V_{MPP} (Fig. 3c). This discrepancy arises because the MEP is jointly determined by η_{ele} and $\eta_{thermal}$, as the TV characteristic causes $\eta_{thermal}$ to also vary with voltage. V_{MEP} decreases and diverges further from V_{MPP} with rising C, as $\frac{d\eta_{thermal}}{dV}$ increases due to the growth of $\frac{dT_{sem}}{dV}$ at elevated C (Supplementary Fig. 10). The SPCM is unable to accurately predict the MEP. V_{MEP} in the SPCM remains identical to V_{MPP} because the constant T_{sem} assumption results in $\eta_{thermal}$ being constant with respect to voltage (Fig. 3d). These findings emphasize the pivotal role of the FRCM in guiding the optimization of η_{total}, as the core of optimizing lies in maximizing η_{total} at the MEP ($\eta_{total-MEP}$).

6. General principles for optimizing $\eta_{total\text{-}MEP}$ through heat transfer adjustments

$\eta_{total-MEP}$ under the initial heat transfer conditions—defined as a flow rate of 1 kg/s and H = 500 μm—is analyzed first. The $\eta_{total-MEP}$ declines at high C (gray line in Fig. 4a) and does not exceed 40 %, which can be attributed to two factors. First, $\eta_{ele-MEP}$ consistently decreases with increasing C (gray line in Fig. 4b) due to the rise in T_{sem}. Second, although $\eta_{thermal-MEP}$ increases with C because of the rise in T_{sem} (gray line in Fig. 4c), the potential for high T_{sem} to produce thermal exergy is not fully realized. This is reflected in the significant gap between $T_{outlet-MEP}$ of the HTF and $T_{sem-MEP}$ (T_{gap}), which exceeds 200 K when C > 500 (Fig. 5a). These findings indicate that $\eta_{total-MEP}$ can be optimized by enhancing the heat transfer to reduce T_{sem} or narrow the T_{gap}.

6.1. Reducing $T_{sem-MEP}$

Convective heat transfer plays a dominant role in thermal output (Fig. 2b-c), so two types of methods to enhance convective heat transfer were tested: increasing the HTF flow rate and improving heat transfer without altering the flow rate. The latter can be achieved through approaches such as increasing the heat exchange area [46,47] or reducing the hydraulic diameter (d_e) of the flow channel [48,49]. In this study, the approach of reducing d_e by decreasing H was chosen (Equation (S7)). Both methods effectively reduce $T_{sem-MEP}$ (Fig. 5b, e). However, the decrease in $T_{outlet-MEP}$ when reducing H is modest (Fig. 5c) but becomes pronounced with an increased flow rate (Fig. 5f). Therefore, their effects on T_{gap} and $\eta_{total-MEP}$ are markedly different. Reducing H significantly decreases T_{gap}, which can drop to less than 5 K when H is 50 μm (Fig. 5a), whereas increasing the flow rate has minimal impact on T_{gap} (Fig. 5d). Reducing H enhances $\eta_{total-MEP}$ and strengthens its positive correlation with increasing C (Fig. 4a), allowing η_{total} to exceed 45 % at high C, but increasing flow rate has the opposite effect (Fig. 4d). Both methods lead to a monotonic increase in $\eta_{ele-MEP}$ (Fig. 4b, e) and a monotonic decrease in $\eta_{thermal-MEP}$ (Fig. 4c, f) when C is fixed. Therefore, reducing H enhances

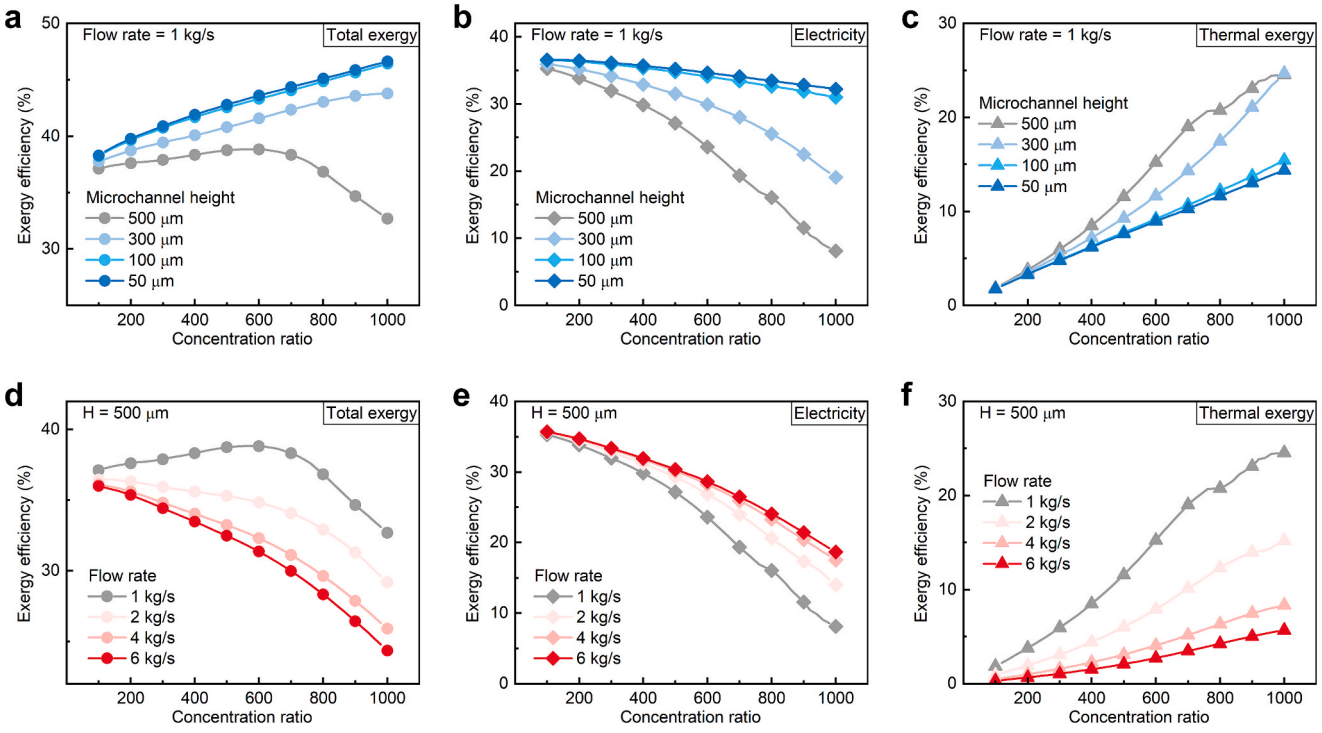

Fig. 4. Variations in exergy efficiencies at MEP when reducing H or increasing flow rate. (a-c) Variations in (a) η_{total}, (b) η_{ele} and (c) $\eta_{thermal}$ at MEP with increasing C when H is reduced, maintaining a flow rate of 1 kg/s. (d-f) Variations in (d) η_{total}, (e) η_{ele} and (f) $\eta_{thermal}$ at MEP with increasing C when the flow rate is increased, with H = 500 μm. E_{g0} is 1.34 eV in (a)-(f), and a data point is recorded for every increment of 20 in C.

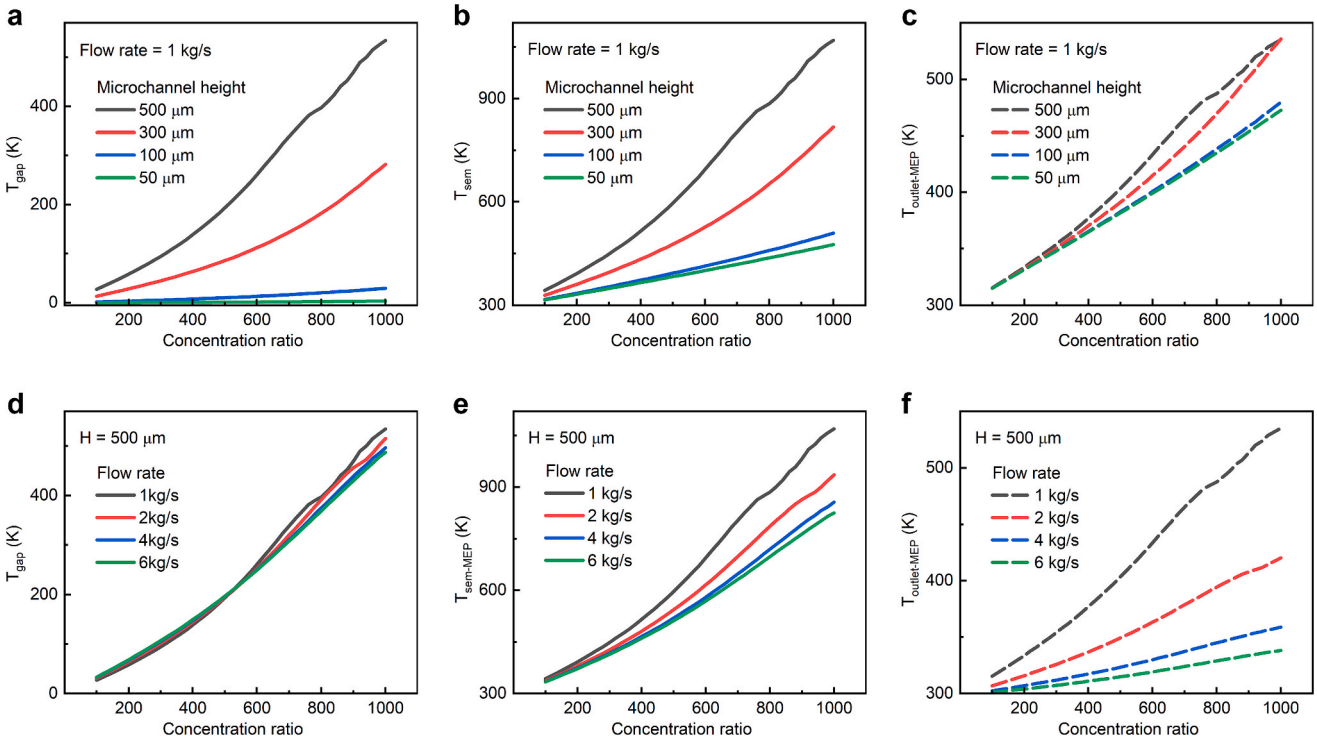

Fig. 5. Variations in T_{gap}, T_{sem} and T_{outlet} at MEP when reducing H or increasing the flow rate. (a-c) Variations in (a) T_{gap}, (b) T_{sem} and (c) T_{outlet} with increasing C when H is reduced, maintaining a flow rate of 1 kg/s. (d-f) Variations in (d) T_{gap}, (e) T_{sem} and (f) T_{outlet} with increasing C when the flow rate is increased, with H = 500 μm. E_{g0} is 1.34 eV in (a)-(f), and a data point is recorded for every increment of 20 in C.

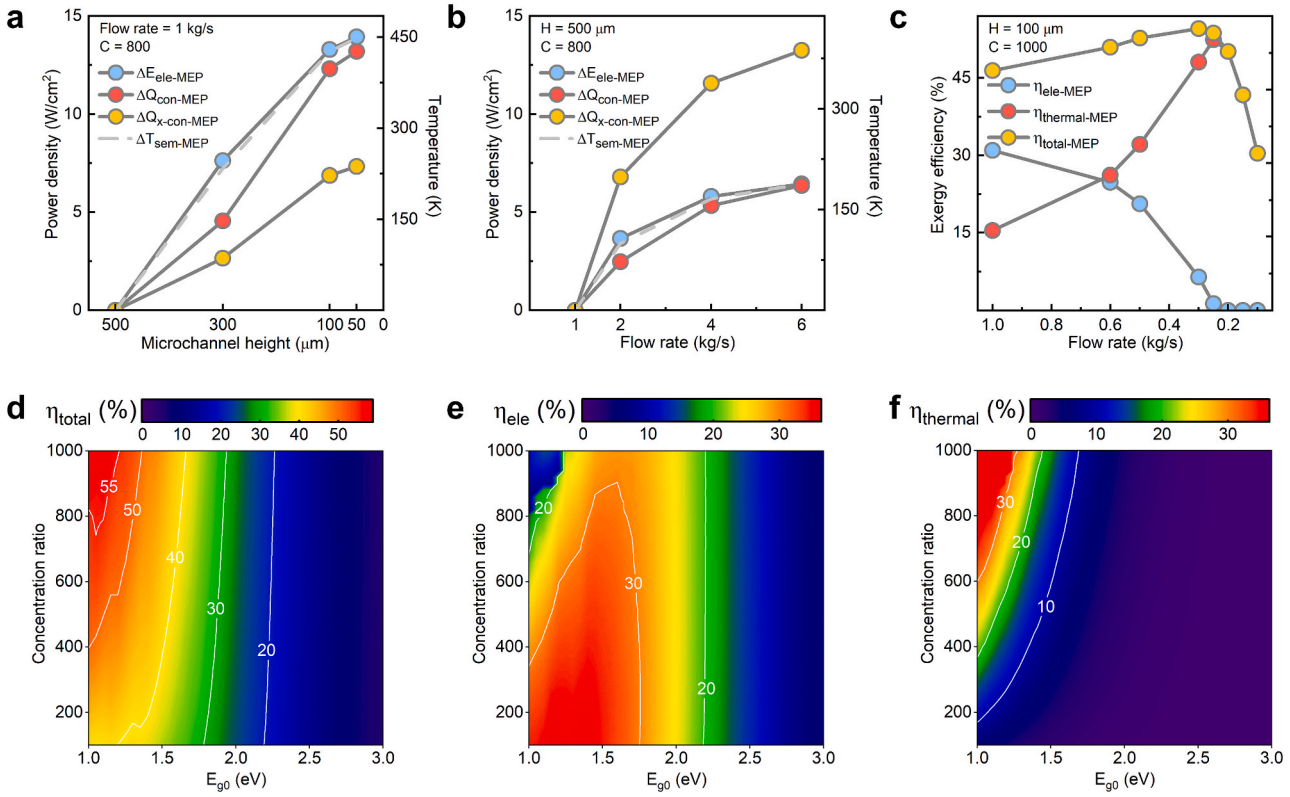

Fig. 6. Theoretical limit of η_{total} and achievable η_{total}. (a, b) $\Delta E_{ele-MEP}$, $\Delta Q_{x-con-MEP}$, $\Delta Q_{con-MEP}$, and $\Delta T_{sem-MEP}$ after (a) reducing H and (b) increasing the flow rate at C = 800. (c) Changes in exergy efficiencies as the flow rate is reduced with H = 100 μm. (d-f) (d) η_{total}, (c) η_{ele}, and (f) $\eta_{thermal}$ at the MEP of the CPV/T system. The flow rate is 0.6 kg/s and H = 100 μm in (d)-(f).

$\eta_{total-MEP}$ because the rise in electricity at MEP ($\Delta E_{ele-MEP}$) exceeds the reduction in thermal exergy at MEP ($\Delta Q_{x-con-MEP}$, Fig. 6a). Conversely, $\Delta E_{ele-MEP}$ is smaller than $\Delta Q_{x-con-MEP}$ (Fig. 6b) when increasing the flow rate.

A larger $\Delta E_{ele-MEP}$ than $\Delta Q_{x-con-MEP}$ and the increase in $\eta_{total-MEP}$ appear to be associated with the narrowing of T_{gap} when reducing $T_{sem-MEP}$. This relationship arises because both the relative magnitudes of $\Delta Q_{x-con-MEP}$ and $\Delta E_{ele-MEP}$ and the change in T_{gap} are determined by the reduction in $T_{sem-MEP}$ ($\Delta T_{sem-MEP}$) and in $T_{outlet-MEP}$ ($\Delta T_{outlet-MEP}$) after heat transfer adjustments. Specifically, $\Delta T_{sem-MEP}$ directly determines $\Delta E_{ele-MEP}$, and the reduction in thermal energy at MEP ($\Delta Q_{con-MEP}$) is close to $\Delta E_{ele-MEP}$ (Fig. 6a-b), which is governed by the intrinsic properties of semiconductors (Supplementary Fig. 11). However, $\Delta Q_{x-con-MEP}$ depends not only on $\Delta Q_{con-MEP}$ but also on $\Delta T_{outlet-MEP}$, as $\Delta T_{outlet-MEP}$ controls changes in the efficiency of the Carnot cycle (η_{Carnot}), which dictates the conversion efficiency of thermal energy to exergy. $\Delta T_{outlet-MEP}$ is small when reducing H (Supplementary Fig. 12a), resulting in only a slight decline in η_{Carnot}. Consequently, $\Delta Q_{x-con-MEP}$ is less than $\Delta Q_{con-MEP}$ and $\Delta E_{ele-MEP}$ (Fig. 6a, $\Delta Q_{x-con-MEP}$ can be approximated as $\Delta Q_{con-MEP} \times \eta_{Carnot}$ under this condition). The smaller $\Delta T_{outlet-MEP}$ compared to $\Delta T_{sem-MEP}$ also drives a reduction in T_{gap}, linking the narrowing of T_{gap} to the increase in $\eta_{total-MEP}$. Conversely, when increasing the flow rate, $\Delta T_{outlet-MEP}$ is approximately equal to $\Delta T_{sem-MEP}$ (Supplementary Fig. 12b), leading to a nearly unchanged T_{gap}. Therefore, $\Delta Q_{x-con-MEP}$ exceeds $\Delta Q_{con-MEP}$ and $\Delta E_{ele-MEP}$ due to the significant decline in η_{Carnot} (Fig. 6b), causing the decrease in $\eta_{total-MEP}$. Overall, for the strategy to enhance $\eta_{total-MEP}$ through reducing $T_{sem-MEP}$, a simultaneous decrease in T_{gap} is a necessary condition. Therefore, the upper limit of the $T_{sem-MEP}$ redcution strategy is reached when T_{gap} is exactly zero after the heat transfer adjustment, as further simultaneous reductions in $T_{sem-MEP}$ and T_{gap} become unavailable. This is supported by the observation that reducing H from 100 μm to 50 μm results in only a slight increase in $\eta_{total-MEP}$ (Fig. 4a), as T_{gap} is already sufficiently small at H = 100 μm (< 30 K at C = 1000, Fig. 5a). The different relative magnitudes of $\Delta T_{sem-MEP}$ and $\Delta T_{outlet-MEP}$ in the two types of heat transfer adjustments are attributed to their distinct impacts on the convective heat transfer coefficient, which are discussed in detail in Supplementary Note 6 and Supplementary Figs. 13-17.

6.2. Increasing $T_{sem-MEP}$

The preceding discussion is based on the premise of reducing $T_{sem-MEP}$ to improve $\eta_{ele-MEP}$. However, a reverse analysis of Fig. 4d reveals that increasing $T_{sem-MEP}$ can also enhance $\eta_{total-MEP}$. Although $\eta_{ele-MEP}$ decreases with rising $T_{sem-MEP}$ as the flow rate decreases from 6 kg/s to 1 kg/s (Fig. 4e, Fig. 5e), $\eta_{total-MEP}$ increases because the rise in $\eta_{thermal-MEP}$ outweighs the decline in $\eta_{ele-MEP}$ (Fig. 4f). Reducing the flow rate to 0.6 kg/s further validates the effectiveness of the $T_{sem-MEP}$ increase strategy (Supplementary Fig. 18). Minimizing T_{gap} is also crucial for this strategy, as it facilitates the conversion of high $T_{sem-MEP}$ into thermal exergy, thereby amplifying the dominance of the increase in $\eta_{thermal-MEP}$ over the decrease in $\eta_{ele-MEP}$. The necessity of narrowing T_{gap} suggests combining reducing the flow rate with decreasing H. Decreasing H to 100 μm can effectively narrow T_{gap} to near zero under reduced flow rate conditions (Supplementary Fig. 19), enabling the combined method (Fig. 6c) to significantly outperform the approach of reducing the flow rate alone (Supplementary Fig. 18). Under this condition, the ideal CPV/T system achieves a peak $\eta_{total-MEP}$ value of 54.6 % when the flow rate is reduced to 0.3 kg/s at C = 1000. The peak value also defines the theoretical upper limit of the $T_{sem-MEP}$ increase strategy at C = 1000. Further reductions in flow rate lead to declines in $\eta_{thermal-MEP}$ and $\eta_{total-MEP}$, despite $T_{sem-MEP}$ continuing to increase and T_{gap} remaining near zero. This occurs because E_{rad} and Q_{rad} gradually dominate at higher $T_{sem-MEP}$, thereby compressing $Q_{con-MEP}$ (Supplementary Fig. 20).

7. Theoretical limit of η_{total} and achievable η_{total}

The peak η_{total} value of 54.6 % highlights that the $T_{sem-MEP}$ increase strategy provides a higher theoretical upper limit compared to the $T_{sem-MEP}$ reduction strategy (Fig. 6c). The latter achieves a theoretical maximum η_{total} of 46.4 % at C = 1000 (Fig. 4a) under conditions with H = 50 μ m and T_{gap} near zero. Consequently, the theoretical limit achieved by the $T_{sem-MEP}$ increase strategy defines the theoretical limit for η_{total} of the ideal CPV/T system, which can be reached by simultaneously reducing T_{gap} to near zero and appropriately elevating $T_{sem-MEP}$ through precise heat transfer adjustments.

Although the value of 54.6 % can be regarded as the theoretical limit for η_{total} of the ideal CPV/T system with E_{g0} = 1.34 eV, C = 1000, and e = 1, achieving this limit presents significant challenges due to the extremely high T_{sem} (1144.4 K, Supplementary Fig. 19), which far exceeds the temperature tolerance of existing CPVs. η_{ele} also drops to zero under such a high T_{sem}. However, by carefully managing the reduction in flow rate, η_{total} can be substantially improved while preventing device overheating. For example, when the flow rate is reduced to 0.6 kg/s instead of 0.3 kg/s with H = 100 μm, an impressive $\eta_{total-MEP}$ of 50.9 % is achieved (Fig. 6c). Meanwhile, $T_{sem-MEP}$ (601.7 K) remains well within the temperature tolerance of CPVs [25], and η_{ele} retains an excellent value of 24.7 %. Therefore, we adopted heat transfer conditions of H = 100 μm and a flow rate of 0.6 kg/s to explore more achievable theoretical η_{total} over a broader range. C varied from 100 to 1000, and E_{g0} was set between 1 eV and 3 eV, encompassing most PVs with practical applications. The combination of reduced H and decreased flow rate ensures excellent η_{total} performance. Specifically, η_{total} exceeds 40 % even at C slightly above 150 when E_{g0} < 1.35 eV, and surpasses 55 % at higher C (Fig. 6d), which is a significant advancement compared to the prediction of previous models. The small H ensures that T_{gap} remains below 33 K (Supplementary Fig. 21a), which ensures that η_{total} remains positively correlated with higher C and lower E_{g0} (Fig. 6d, 4a). Furthermore, the reduced H effectively limits the rise of T_{sem} (Fig. 5b). For most E_{g0} and C values, T_{sem} remains below 600 K (Supplementary Fig. 21b), with a maximum T_{sem} of less than 710 K, which is well within the tolerance of high-temperature CPVs. The relatively low T_{sem} ensures that η_{ele} does not significantly decrease with rising C (Fig. 6e). Consequently, η_{ele} contributes over 80 % to η_{total} in most regions, and even in regions where T_{sem} exceeds 700 K, its contribution remains above 30 % (Supplementary Fig. 22). However, in the blue region at the upper left corner of Fig. 6e, T_{sem} exceeds 710 K (with a maximum of 775 K), and the contribution of η_{ele} drops below 30 %, despite η_{total} continuing to increase with higher C and lower E_{g0}. This occurs because the same flow rate was applied for all C and E_{g0} for comparison. Nonetheless, higher C and lower E_{g0} in the blue region require larger flow rate due to the greater thermal source power. As shown in Supplementary Fig. 23, increasing the flow rate from 0.6 kg/s to 1 kg/s effectively narrows the blue area and increases the contribution rate of η_{ele}. This principle of flow rate matching also illustrates that 0.6 kg/s is excessive in regions where E_{g0} > 1.34 eV or where E_{g0} < 1.34 eV but C is relatively low. In these regions, $\eta_{thermal}$ and η_{total} (Fig. 6d, f) can be further improved by reducing the flow rate to appropriately increase $T_{sem-MEP}$.

The theoretical η_{total} of CPV/T systems demonstrates a substantial improvement compared to the Shockley-Queisser limit of PV ($\eta_{Shockley}$), even when the blue region in Fig. 6e is excluded. The relative increase ($\frac{\eta_{total}-\eta_{Shockley}}{\eta_{Shockley}}$) rises with higher C and lower E_{g0} (Supplementary Fig. 24a), exceeding 30 % for E_{g0} < 1.5 eV when C > 460 and reaching 40 %–78 % around E_{g0} = 1.34 eV when C > 600, which corresponds to an absolute increase of 15 % to 24 % (Supplementary Fig. 24b). The highest theoretical η_{total} within the explored range is 56.1 %, observed at E_{g0} = 1.1 eV and C = 880, representing a relative increase of 69.0 % over the Shockley-Queisser limit for the optimal bandgap (33.2 %) [42]. This underscores the remarkable potential of CPV/T systems. If full-spectrum

utilization is considered—converting radiation outside the absorption range of the CPV into thermal energy at T_{outlet}—η_{total} at $E_{g0} = 1.1$ eV and C = 880 increases to 62.5 %. Notably, this study focuses exclusively on single-junction devices. The implementation of multi-junction CPV is expected to further enhance the theoretical η_{total}.

8. Model generalizability and future research

8.1. Model generality and practical applicability

The FRCM exhibits strong generality. Although the FRCM is applied to ideal CPV/T devices in this study, it reserves interfaces for both CB and TE of practical CPV/T systems, enabling accurate modeling and facilitating design and optimization of real-world devices to enhance their η_{total}. Several key interfaces are introduced below:

(1) Non-radiative recombination. In practical materials, non-radiative recombination cannot be neglected. It not only affects CB but also acts as a thermal source participating in TE through CB–TE coupling [14]. We have reserved an interface to accommodate non-radiative recombination (see E_{nonrad} in Eqs. (3) and (8)), allowing non-radiative recombination characteristics of real materials to be incorporated.
(2) Temperature-dependent parameters. For instance, the temperature dependence of the bandgap and the radiative recombination coefficient in real materials can be directly incorporated into the FRCM (Equations (S1) and (S2)).
(3) TE. FRCM includes dedicated interfaces for conductive, convective, and radiative heat transfer (Eq. (8)), enabling accurate modeling tailored to the heat transfer conditions of practical CPV/T devices. In addition, the FRCM can also be incorporated as a CB–TE coupling module into commercial multiphysics platforms such as Fluent or COMSOL, leveraging their mature capabilities in heat transfer, multiphase flow. This is also the direction of our future work.

In summary, the FRCM can support the modeling and optimization of practical CPV/T systems. For example, it can determine the tuning direction of the temperature dependence of the bandgap in material design, the optimization of thermal management strategies of practical devices, and aid in selecting thermal utilization technologies that align with specific CPV/T devices.

8.2. Current status and future research of practical CPV/T devices

Considering the existing high-temperature CPV technologies and cooling technologies, the high-temperature CPV/T devices proposed in this study are a feasible concept with strong economic viability:

(1) Significant progress has been made in high-temperature CPVs. For instance, some advanced III-V CPVs are now capable of maintaining a η_{ele} of approximately 10 % at 673 K [44]. They are fabricated via chemical vapor deposition (CVD), which is compatible with existing industrial infrastructure. Additionally, the high-temperature performance of emerging solar cells continues to improve—for instance, there are perovskite solar cells that exhibit only a 30 % reduction in η_{ele} at 500 K compared to room temperature operation.
(2) The microchannel dimensions used for cooling in this model (50–500 μm) are common in current industrial applications, [50] although the associated manufacturing costs still require further reduction.
(3) The cost of optical concentrator components is steadily decreasing with the rapid advancement of concentrated solar power technologies [39]

However, the η_{total} of current high-temperature CPV/T devices remain far below the theoretical limit. Many critical challenges remain to be addressed:

(1) Severe non-radiative recombination at elevated temperatures still significantly constrains the photoelectric performance of CPVs. Further advances in defect passivation, interface engineering, and structural optimization are required to suppress recombination and extend device longevity.
(2) The use of tandem semiconductors is expected to further enhance η_{total} of CPV/T systems, and some progress has been reported on tandem devices operating at high temperatures [51]. Nevertheless, achieving high interfacial carrier transport efficiency, efficient thermal conduction between layers, and mechanical compatibility under thermal stress remains a challenge. These issues depend heavily on future advancements in materials and device architecture.
(3) System-level modeling and optimization require further advancement, particularly in the coordinated management of multiple energy flows, including optical, thermal, and electrical energy.
(4) Breakthroughs in more efficient thermal utilization technologies and their integration with CPV/T systems are also expected to make positive contributions to the enhancement of both $\eta_{thermal}$ and η_{total}.

9. Conclusion

We developed an FRCM that couples CB and TE across the entire operating voltage range. This model reveals pronounced TV characteristics in CPV/T systems due to voltage-dependent variations of CB-TE coupling, as validated by experimental data. The TV characteristic substantially influences the IV characteristic and η_{total} of CPV/T systems through CB-TE coupling and results in an MEP that differs from the MPP. In contrast, the traditional SPCM fails to reflect these effects because its constant T_{sem} assumption cannot capture the TV characteristics, thereby leading to inaccuracies. Universal principles for enhancing η_{total} through heat transfer adjustment are identified with FRCM. The $T_{sem-MEP}$ increase strategy is shown to provide a higher upper limit than the $T_{sem-MEP}$ reduction strategy. For both strategies, minimizing T_{gap} emerges as a common criterion for effectively enhancing η_{total}. Based on these principles, we demonstrate that the theoretical limit for η_{total} of the ideal CPV/T system can be reached by simultaneously reducing T_{gap} to near zero and appropriately elevating $T_{sem-MEP}$ through precise heat transfer adjustments. Calculations across a wide range of bandgaps and concentration ratios indicate that the theoretical η_{total} can exceed 56 %. This work deepens the fundamental understanding of CPV/T systems and establishes a robust framework for predicting performance and guiding optimization, providing critical insights for advancing CPV/T technologies toward highly efficient and sustainable energy solutions.

CRediT authorship contribution statement

Yuan Gao: Writing – review & editing, Writing – original draft, Visualization, Validation, Software, Methodology, Investigation, Formal analysis, Conceptualization. **Entao Zhang:** Software, Methodology. **Yin Xie:** Writing – review & editing, Writing – original draft, Visualization. **Xuan Zhu:** Writing – review & editing, Writing – original draft, Visualization. **Chenyu Xu:** Writing – review & editing, Supervision, Resources. **Yanwei Zhang:** Writing – review & editing, Writing – original draft, Supervision, Resources, Funding acquisition, Conceptualization.

Declaration of competing interest

The authors declare that they have no known competing financial

interests or personal relationships that could have appeared to influence the work reported in this paper.

Acknowledgments

This work is supported by the National Natural Science Foundation of China (52341602), Zhejiang Provincial Natural Science Foundation of China under Grant No. LDT23E06014E06, Zhejiang Provincial Natural Science Foundation of China under Grant No. LQ24E060001, National Key Research and Development Project (2023YFC3710800), and the Fundamental Research Funds for the Central Universities (2022ZFJH04).

Appendix A. Supplementary data

Supplementary data to this article can be found online at https://doi.org/10.1016/j.enconman.2025.120266.

Data availability

Data will be made available on request.

References

[1] Anand B, Shankar R, Murugavelh S, Rivera W, Midhun Prasad K, Nagarajan R. A review on solar photovoltaic thermal integrated desalination technologies. Renew Sust Energ Rev 2021;141:110787. https://doi.org/10.1016/j.rser.2021.110787.
[2] Daneshazarian R, Cuce E, Cuce PM, Sher F. Concentrating photovoltaic thermal (CPVT) collectors and systems: Theory, performance assessment and applications. Renew Sust Energ Rev 2018;81:473–92. https://doi.org/10.1016/j.rser.2017.08.013.
[3] Meneses-Rodríguez D, Horley PP, González-Hernández J, Vorobiev YV, Gorley PN. Photovoltaic solar cells performance at elevated temperatures. Sol Energy 2005;78:243–50. https://doi.org/10.1016/j.solener.2004.05.016.
[4] Xu N, JI J, Sun W, Huang W. Comparative study on two photovoltaic and thermal solar moduleds with point-focus Fresnel concentrator. 2015 ISES Solar World Congress (SWC). 2015.
[5] Huang, K. (1988). Solid state physics (Higher Education Press).
[6] Shockley W, Queisser HJ. Detailed balance limit of efficiency of p-n junction solar cells. J Appl Phys 1961;32:510–9. https://doi.org/10.1063/1.1736034.
[7] Dupré O, Vaillon R, Green MA. Physics of the temperature coefficients of solar cells. Sol Energy Mater Sol Cells 2015;140:92–100. https://doi.org/10.1016/j.solmat.2015.03.025.
[8] Zhao J, Wang A, Robinson SJ, Green MA. Reduced temperature coefficients for recent high-performance silicon solar cells. Prog Photovolt Res Appl 1994;2:221–5. https://doi.org/10.1002/pip.4670020305.
[9] Aydin E, Allen TG, De Bastiani M, Xu L, Ávila J, Salvador M, et al. Interplay between temperature and bandgap energies on the outdoor performance of perovskite/silicon tandem solar cells. Nat Energy 2020;5:851–9. https://doi.org/10.1038/s41560-020-00687-4.
[10] Han J, Lu L, Yang H. Numerical evaluation of the mixed convective heat transfer in a double-pane window integrated with see-through a-Si PV cells with low-e coatings. Appl Energy 2010;87:3431–7. https://doi.org/10.1016/j.apenergy.2010.05.025.
[11] Tiwari GN, Mishra RK, Solanki SC. Photovoltaic modules and their applications: a review on thermal modelling. Appl Energy 2011;88:2287–304. https://doi.org/10.1016/j.apenergy.2011.01.005.
[12] Tembhurne S, Nandjou F, Haussener S. A thermally synergistic photo-electrochemical hydrogen generator operating under concentrated solar irradiation. Nat Energy 2019;4:399–407. https://doi.org/10.1038/s41560-019-0373-7.
[13] Peters IM, Buonassisi T. Energy yield limits for single-junction solar cells. Joule 2018;2:1160–70. https://doi.org/10.1016/j.joule.2018.03.009.
[14] Hajjiah A. COMSOL simulation of non-radiative recombination heat and joule heat in CZTSSe thin film solar cells. Micro Nano Struct 2022;168:207313. https://doi.org/10.1016/j.micrna.2022.207313.
[15] Zandi S, Seresht MJ, Khan A, Gorji NE. Simulation of heat loss in $Cu_2ZnSn_4S_xSe_{4-x}$ thin film solar cells: a coupled optical-electrical-thermal modeling. Renew Energy 2022;181:320–8. https://doi.org/10.1016/j.renene.2021.09.035.
[16] Ahmed A, Zhang G, Shanks K, Sundaram S, Ding Y, Mallick T. Performance evaluation of single multi-junction solar cell for high concentrator photovoltaics using minichannel heat sink with nanofluids. Appl Therm Eng 2021;182:115868. https://doi.org/10.1016/j.applthermaleng.2020.115868.
[17] Yuan W, Ji J, Modjinou M, Zhou F, Li Z, Song Z, et al. Numerical simulation and experimental validation of the solar photovoltaic/thermal system with phase change material. Appl Energy 2018;232:715–27. https://doi.org/10.1016/j.apenergy.2018.09.096.
[18] Xu Z, Kleinstreuer C. Concentration photovoltaic–thermal energy co-generation system using nanofluids for cooling and heating. Energy Convers Manag 2014;87:504–12. https://doi.org/10.1016/j.enconman.2014.07.047.
[19] Otanicar T, Chowdhury I, Phelan PE, Prasher R. Parametric analysis of a coupled photovoltaic/thermal concentrating solar collector for electricity generation. J Appl Phys 2010;108:114907. https://doi.org/10.1063/1.3514590.
[20] Singh P, Ravindra NM. Temperature dependence of solar cell performance—an analysis. Sol Energy Mater Sol Cells 2012;101:36–45. https://doi.org/10.1016/j.solmat.2012.02.019.
[21] Khan SA, Bicer Y, Koç M. Design and analysis of a multigeneration system with concentrating photovoltaic thermal (CPV/T) and hydrogen storage. Int J Hydrogen Energy 2020;45:3484–98. https://doi.org/10.1016/j.ijhydene.2018.12.047.
[22] Lin L, Tian Y, Luo Y, Chen C, Jiang L. A novel solar system integrating concentrating photovoltaic thermal collectors and variable effect absorption chiller for flexible co-generation of electricity and cooling. Energy Convers Manag 2020;206:112506. https://doi.org/10.1016/j.enconman.2020.112506.
[23] Zhang Z, Hu Z, Xu H, Dai X, Wang J, Jiao W, et al. Theoretical analysis of a solar-powered multi-effect distillation integrated with concentrating photovoltaic/thermal system. Desalination 2019;468:114074. https://doi.org/10.1016/j.desal.2019.114074.
[24] Zhao Y, Xu M, Huang X, Lebeau J, Li T, Wang D, et al. Toward high efficiency at high temperatures: recent progress and prospects on InGaN-Based solar cells. Mater Today Energy 2023;31:101229. https://doi.org/10.1016/j.mtener.2022.101229.
[25] Huang X, Li W, Fu H, Li D, Zhang C, Chen H, et al. High-temperature polarization-free III-nitride solar cells with self-cooling effects. ACS Photonics 2019;6:2096–103. https://doi.org/10.1021/acsphotonics.9b00655.
[26] Williams JJ, McFavilen H, Fischer AM, Ding D, Young SR, Vadiee E, et al. Development of a high-bandgap high temperature III-nitride solar cell for integration with concentrated solar power technology. 2016 IEEE 43rd Photovoltaic Specialists Conference (PVSC). 2016.
[27] Dong Z, Li W, Wang H, Jiang X, Liu H, Zhu L, et al. High-temperature perovskite solar cells. Sol RRL 2021;5:2100370. https://doi.org/10.1002/solr.202100370.
[28] Miao J, Meng B, Ding Z, Liu J, Wang L. Organic solar cells based on small molecule donors and polymer acceptors operating at 150 °C. J Mater Chem A 2020;8:10983–8. https://doi.org/10.1039/d0ta02865g.
[29] Afshari H, Sourabh S, Chacon SA, Whiteside VR, Penner RC, Rout B, et al. FACsPb triple halide perovskite solar cells with thermal operation over 200 °C. ACS Energy Lett 2023;8:2408–13. https://doi.org/10.1021/acsenergylett.3c00551.
[30] Helmers H, Bett AW, Parisi J, Agert C. Modeling of concentrating photovoltaic and thermal systems. Prog Photovolt Res Appl 2014;22:427–39. https://doi.org/10.1002/pip.2287.
[31] Yin E, Li Q. Multi-objective optimization of a concentrated spectrum splitting photovoltaic-thermoelectric hybrid system. Appl Therm Eng 2023;219:119518. https://doi.org/10.1016/j.applthermaleng.2022.119518.
[32] Radwan A, Ahmed M. The influence of microchannel heat sink configurations on the performance of low concentrator photovoltaic systems. Appl Energy 2017;206:594–611. https://doi.org/10.1016/j.apenergy.2017.08.202.
[33] Passler R. Parameter sets due to fittings of the temperature dependencies of fundamental bandgaps in semiconductors. Phys Status Solidi B 1999;216:975. https://doi.org/10.1002/%28SICI%291521-3951%28199912%29216%3A2<975%3A%3AAID-PSSB975>3.0.CO%3B2-N.
[34] Passler R. Basic model relations for temperature dependencies of fundamental energy gaps in semiconductors. Phys Status Solidi B 1997;200:155–72. https://doi.org/10.1002/1521-3951(199703)200:1<155::Aid-pssb155>3.0.Co;2-3.
[35] Giteau M, de Moustier E, Suchet D, Esmaielpour H, Sodabanlu H, Watanabe K, et al. Identification of surface and volume hot-carrier thermalization mechanisms in ultrathin GaAs layers. J Appl Phys 2020;128:193102. https://doi.org/10.1063/5.0027687.
[36] Guillemoles J-F, Kirchartz T, Cahen D, Rau U. Guide for the perplexed to the Shockley–Queisser model for solar cells. Nat Photonics 2019;13:501–5. https://doi.org/10.1038/s41566-019-0479-2.
[37] Yang, S., and Tao, W. (2006). Heat transfer (Higher Education Press).
[38] Mittapally R, Majumder A, Reddy P, Meyhofer E. Near-field thermophotovoltaic energy conversion: Progress and opportunities. Phys Rev Appl 2023;19:037002. https://doi.org/10.1103/PhysRevApplied.19.037002.
[39] Valenzuela L, López-Martín R, Zarza E. Optical and thermal performance of large-size parabolic-trough solar collectors from outdoor experiments: a test method and a case study. Energy 2014;70:456–64. https://doi.org/10.1016/j.energy.2014.04.016.
[40] Yu B, Jiang Q, He W, Liu S, Zhou F, Ji J, et al. Performance study on a novel hybrid solar gradient utilization system for combined photocatalytic oxidation technology and photovoltaic/thermal technology. Appl Energy 2018;215:699–716. https://doi.org/10.1016/j.apenergy.2018.02.017.
[41] Xu L, Liu W, Liu H, Ke C, Wang M, Zhang C, et al. Heat generation and mitigation in silicon solar cells and modules. Joule 2021;5:631–45. https://doi.org/10.1016/j.joule.2021.01.012.
[42] Rühle S. Tabulated values of the Shockley–Queisser limit for single junction solar cells. Sol Energy 2016;130:139–47. https://doi.org/10.1016/j.solener.2016.02.015.
[43] Perl EE. Material science for high-efficiency photovoltaics: from advanced optical coatings to cell design for high-temperature applications. Doctor of Philosophy (University of California Santa Barbara); 2016.
[44] Perl EE, Simon J, Geisz JF, Lee ML, Friedman DJ, Steiner MA. Measurements and modeling of III-V solar cells at high temperatures up to 400 °C. IEEE J Photovolt 2016;6:1345–52. https://doi.org/10.1109/jphotov.2016.2582398.

[45] Perl EE, Kuciauskas D, Simon J, Friedman DJ, Steiner MA. Identification of the limiting factors for high-temperature GaAs, GaInP, and AlGaInP solar cells from device and carrier lifetime analysis. J Appl Phys 2017;122:233102. https://doi.org/10.1063/1.5003631.
[46] Mahesh P, Kumar KK, Balasubramanian K, Chandramohan VP, Lee PS, Kong CC. Comparative study of elliptical fin microchannel over oblique micro-fin heat sinks. Asia Pac J Chem Eng 2022;17:e2834.
[47] Soleimani S, Eckels S. Multi-objective optimization of 3D micro-fins using NSGA-II. Int J Heat Mass Transf 2022;197:123315. https://doi.org/10.1016/j.ijheatmasstransfer.2022.123315.
[48] Zhang HY, Pinjala D, Wong TN, Toh KC, Joshi YK. Single-phase liquid cooled microchannel heat sink for electronic packages. Appl Therm Eng 2005;25:1472–87. https://doi.org/10.1016/j.applthermaleng.2004.09.014.
[49] Radwan A, Ookawara S, Ahmed M. Thermal management of concentrator photovoltaic systems using two-phase flow boiling in double-layer microchannel heat sinks. Appl Energy 2019;241:404–19. https://doi.org/10.1016/j.apenergy.2019.03.017.
[50] Lee P-S, Garimella SV, Liu D. Investigation of heat transfer in rectangular microchannels. Int J Heat Mass Transf 2005;48:1688–704. https://doi.org/10.1016/j.ijheatmasstransfer.2004.11.019.
[51] Perl EE, Simon J, Geisz JF, Olavarria W, Young M, Duda A, et al. Development of high-bandgap AlGaInP solar cells grown by organometallic vapor-phase epitaxy. IEEE J Photovolt 2016;6:770–6. https://doi.org/10.1109/jphotov.2016.2537543.